GAS-PHASE STRUCTURE AND RELATIVE STABILITY OF PROTON-BOUND HOMO- AND HETEROCHIRAL CLUSTERS OF TETRA-AMIDE MACROCYCLES WITH AMINES

Caterina FRASCHETTI[1], Marco PIERINI[2,*], Claudio VILLANI[3], Francesco GASPARRINI[4], Antonello FILIPPI[5] and Maurizio SPERANZA[6,*]

Dipartimento di Chimica e Tecnologie del Farmaco, Universita "La Sapienza", 00185 Roma, Italy; e-mail: [1] caterina.fraschetti@uniroma1.it, [2] marco.pierini@uniroma1.it, [3] claudio.villani@uniroma1.it, [4] francesco.gasparrini@uniroma1.it, [5] antonello.filippi@uniroma1.it, [6] maurizio.speranza@uniroma1.it

Received July 3, 2008
Accepted September 8, 2008
Published online February 14, 2009

The structure, stability, and CID pattern of proton-bound homochiral and heterochiral complexes, formed in the gas phase by the combination of two molecules of a chiral macrocyclic tetra-amide and an amine B, i.e. CH_3NH_2, $(CH_3)_2NH$, or (*S*)-(–)-1-phenylethylamine, have been examined by ESI-ITMS-CID mass spectrometry. With B = CH_3NH_2, the CID pattern is characterized by the predominant loss of B, accompanied by a much less extensive release of one tetra-amide molecule. With (*S*)-(–)-1-phenylethylamine, loss of a tetra-amide molecule efficiently competes with loss of B. Finally, with $(CH_3)_2NH$, loss of a tetra-amide molecule predominates over loss of B. No appreciable isotope and chiral guest configuration effects have been detected in the fragmentation of the homochiral complexes. A distinct configurational effect has been appreciated in the CID of the homo- and the heterochiral complexes with all amines used. The results of this study have been discussed in the light of semi-empirical computational evidence. The differences in the CID patterns of the homo- and the heterochiral complexes have been rationalized in terms of structural factors and of the basicity of amine B.

Keywords: Diastereoselectivity; Collision-induced dissociation; **S**upramolecular isomers; Amines; Chiral clusters; Mass spectrometry; Gas-phase chiral recognition.

Enzymes are macromolecular assemblies of protein biopolymers that make up the machinery whose structures and dynamics enable and support life functions. An important class of life's supermolecules are noncovalent guest/host complexes where the guest molecule, whose chemistry is of direct interest, is selectively embodied into the host macromolecular structure and modified catalytically at a specific "active site"[1–4]. Indeed, a key supramolecular feature of enzymes is their capacity for "molecular recogni-

Collect. Czech. Chem. Commun. 2009, Vol. 74, No. 2, pp. 275–297

doi:10.1135/cccc2008155

tion". According to this property, the binding and admission to the active site by a particular molecular guest is extremely selective and is based on the enzyme's ability to recognize the guest's size, shape, and chemical characteristics. A significant role is also played by the extensive desolvation of guest molecule entering the receptor cavity which not only favours its uptake, but also greatly enhances its reactivity[5].

The structure and action of enzymes has provided chemists with both a stimulus and an inspiration to design "synthetic enzymes" to provide exemplars for understanding the amazing properties of natural enzymes and for attempting to reproduce them for practical applications. An important step towards the elucidation of enzyme mechanisms requires a comprehensive kinetic study on simplified models under conditions, like the gas phase, where the noncovalent interactions in the guest/host complex are not perturbed by medium effects[6].

Macrocyclic amides form a group of synthetic receptors that gained some attention in recent gas phase studies[7,8]. Interest in this category of macrocyclic hosts comes from the properties of their amido groups in dipolar or H-bonding interactions, the carbonyl acting as a dipole donor and a H-bond acceptor and the N–H as a dipole acceptor and a H-bond donor.

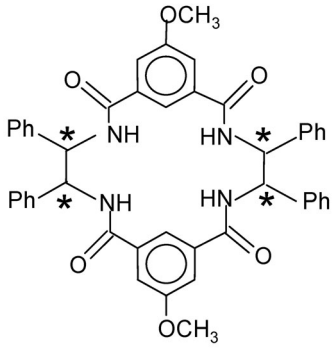

***(R)*-M^H** (* conf. *R*)
***(S)*-M^H** (* conf. *S*)

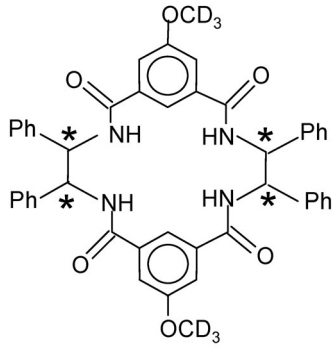

***(R)*-M^D** (* conf. *R*)
***(S)*-M^D** (* conf. *S*)

B= CH_3NH_2 $(CH_3)_2NH$

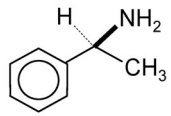

CHART 1

Molecular mechanics calculations indicate that, according to the spatial disposition of their phenyl rings, the macrocyclic tetra-amides of Chart 1 may assume diverse stable conformations classified as equatorial-equatorial (*eq-eq*), axial-axial (*ax-ax*) and axial-equatorial (*ax-eq*), following a decreasing stability order (Chart 2)[8]. In both *eq-eq* and *ax-ax* geometries the macrocycle has a *C*2-symmetric folded structure with a concave and a convex sides (face F1 and F2, respectively).

The structure, stability, and reactivity of proton-bound homochiral and heterochiral complexes between the chiral tetra-amide macrocycle (***R***)-$\mathbf{M^H}$ of Chart 1 and the enantiomers of the ethyl esters of many amino acids A^R and A^S have been investigated in the gas phase by ESI-FT-ICR and ESI-ITMS-CID mass spectrometry[7,8]. Some insights into the relative stability of $[(\boldsymbol{R})\text{-}\mathbf{M^H}\cdot H\cdot A^R]^+$ and $[(\boldsymbol{R})\text{-}\mathbf{M^H}\cdot H\cdot A^S]^+$ was obtained by using Cooks' approach which is based on the collision induced dissociation (CID) of the corresponding three-body $[((\boldsymbol{R})\text{-}\mathbf{M^H})_2\cdot H\cdot A^R]^+$ and $[((\boldsymbol{R})\text{-}\mathbf{M^H})_2\cdot H\cdot A^S]^+$ adducts[9–16]. Their CID patterns are characterized by the exclusive formation of the $[(\boldsymbol{R})\text{-}\mathbf{M^H}\cdot H\cdot A^R]^+$ (or $[(\boldsymbol{R})\text{-}\mathbf{M^H}\cdot H\cdot A^S]^+$) and $[((\boldsymbol{R})\text{-}\mathbf{M^H})_2\cdot H]^+$ fragments in proportions which depend on the relative stability and the collision energies. At equal collision energies, the homochiral $[(\boldsymbol{R})\text{-}\mathbf{M^H}\cdot H\cdot A^R]^+$ complexes are found to be more stable than the corresponding heterochiral $[(\boldsymbol{R})\text{-}\mathbf{M^H}\cdot H\cdot A^S]^+$ ones.

Kinetic analysis of the displacement of the A guest from the diastereomeric $[(\boldsymbol{R})\text{-}\mathbf{M^H}\cdot H\cdot A]^+$ complexes by the enantiomers of 2-aminobutane

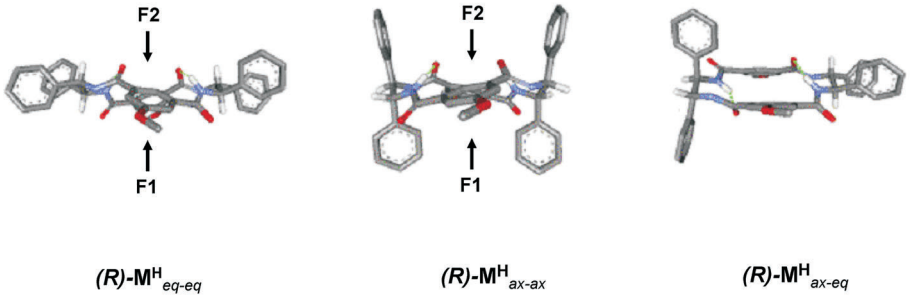

CHART 2

In the *eq-eq* and *ax-ax* geometries, macrocycle (***R***)-$\mathbf{M^H}$ presents a concave side, F1, and a convex one, F2. Alternate and diverging CO and NH groups are located on the outer margins of F1, whereas the same, but now converging functionalities are placed on the central folding of F2. Such molecular framework, reminding the structure of a saddle roof, is stabilized by two strong H-bonds between two facing amide moieties

provided compelling evidence that the most stable *eq-eq* conformer of (***R***)-$\mathbf{M^H}$ ((***R***)-$\mathbf{M^H}_{eq\text{-}eq}$ in Chart 2) may acquire in the gas phase the *ax-ax* conformation by induced fit on complexation with the A guest. This leads to the co-existence in the gas phase of stable [(***R***)-$\mathbf{M^H}_{eq\text{-}eq}$·H·A]$^+$ and [(***R***)-$\mathbf{M^H}_{ax\text{-}ax}$·H·A]$^+$ structures, in proportions depending on the configuration of A and characterized by different stability and reactivity towards the enantiomers of 2-aminobutane. Occurrence of the [(***R***)-$\mathbf{M^H}_{ax\text{-}eq}$·H·A]$^+$ conformers was excluded on the basis of their much lower stability.

This intriguing picture prompted us to widen the investigation to the proton-bound homochiral [((***R***)-$\mathbf{M^H}$)$_2$·H·B]$^+$ and [((***S***)-$\mathbf{M^D}$)$_2$·H·B]$^+$ complexes and the heterochiral [(***R***)-$\mathbf{M^H}$·(***S***)-$\mathbf{M^D}$·H·B]$^+$ one co-generated in a ITMS by electrospraying methanolic solutions containing an amine B, i.e. CH_3NH_2, $(CH_3)_2NH$, or (*S*)-(–)-1-phenylethylamine, and the quasi-racemate of the chiral tetra-amide macrocyclic host, i.e. [(***R***)-$\mathbf{M^H}$]/[(***S***)-$\mathbf{M^D}$] = 1 (Chart 1)[17,18]. Control experiments have been carried out by using the proton-bound [((***S***)-$\mathbf{M^H}$)$_2$·H·B]$^+$, [((***R***)-$\mathbf{M^D}$)$_2$·H·B]$^+$, and [(***S***)-$\mathbf{M^H}$·(***R***)-$\mathbf{M^D}$·H·B]$^+$ complexes, obtained from methanolic solutions of B together with the [(***S***)-$\mathbf{M^H}$]/[(***R***)-$\mathbf{M^D}$] = 1 quasi-racemate. For the sake of simplicity, the proton-bound homochiral [((***R***)-$\mathbf{M^H}$)$_2$·H·B]$^+$ and [((***S***)-$\mathbf{M^H}$)$_2$·H·B]$^+$ complexes will be denoted as [($\mathbf{M^X}$)$_2$·H·B]$^+$ (X = H), the homochiral [((***R***)-$\mathbf{M^D}$)$_2$·H·B]$^+$ and [((***S***)-$\mathbf{M^D}$)$_2$·H·B]$^+$ ones as [($\mathbf{M^X}$)$_2$·H·B]$^+$ (X = D), and the heterochiral [(***R***)-$\mathbf{M^H}$·(***S***)-$\mathbf{M^D}$·H·B]$^+$ and [(***S***)-$\mathbf{M^H}$·(***R***)-$\mathbf{M^D}$·H·B]$^+$ complexes as [$\mathbf{M^H}$·$\mathbf{M^D}$·H·B]$^+$. Analysis of their CID patterns under exactly the same experimental conditions may provide some information on: (i) the isotope effect on the fragmentation process (by comparing the CID spectra of [($\mathbf{M^X}$)$_2$·H·B]$^+$ (X = H, D)), (ii) the effects of a chiral guest, i.e. (*S*)-(–)-1-phenylethylamine, on the CID spectra of [($\mathbf{M^X}$)$_2$·H·B]$^+$ (X = H, D), (iii) the effects of the host configuration (by comparing the CID spectra of the homochiral [($\mathbf{M^X}$)$_2$·H·B]$^+$ (X = H, D) adducts with that of the heterochiral [$\mathbf{M^H}$·$\mathbf{M^D}$·H·B]$^+$ ones), and (iv) the structural features of the involved species with the aid of docking simulations.

EXPERIMENTAL

Mass Spectrometric Experiments

The ESI-ITMS-CID experiments were performed on an Applied Biosystems Linear Ion Trap API 2000 mass spectrometer equipped with an electrospray ionization (ESI) source and a syringe pump. Operating conditions of the ESI source are the followings: ion spray voltage +5.5 kV, sheath gas 34 psi, nebulizer gas 15 psi, focusing rod offset (IS) +10 V, orifice plate +35 V, capillary temperature 210 °C. Methanolic solutions are infused via a syringe pump at a flow rate of 10 μl/min. ESI of equimolar solutions (1×10^{-5} mol/l) containing two pseudo-

enantiomers of the macrocyclic host, i.e. either [(***R***)-$\mathbf{M^H}$] = [(***S***)-$\mathbf{M^D}$] or [(***S***)-$\mathbf{M^H}$] = [(***R***)-$\mathbf{M^D}$] together with an equimolar amount of the hydrochloride of amine B, leads to the formation of appreciable amounts of the corresponding proton-bound [$(\mathbf{M^X})_2$·H·B]$^+$ (X = H, D) and [$\mathbf{M^H}$·$\mathbf{M^D}$·H·B]$^+$ complexes in the approximate 1:1:2 ratio. After broad-band ejection of the accompanying ions (mass resolution 1 amu), the isolated [$(\mathbf{M^X})_2$·H·B]$^+$ (X = H, D) and [$\mathbf{M^H}$·$\mathbf{M^D}$·H·B]$^+$ adducts were individually submitted to CID by collisions with N_2 gas (nominal pressure in collision chamber, 1.4×10^{-5} torr). The survivor precursor and its product ions were accumulated in the linear trap (LIT) of the instrument (fill time of the trap 20 ms, scan rate 1000 amu/s) to improve the signal-to-noise ratio and eventually detected. The CID collision energy (E_{lab} = 5–20 eV) is calculated from the difference in volts between –IS and collision cell rod offset. The relative abundance of fragments results from area of peaks of the spectra acquired in profile mode. In each acquisition the final spectra are the average of about 70 scans, each consisting of two microscans. Standard deviation of relative ion abundances ±10%.

Computational Details

All calculations were performed with software packages running on a PC equipped with Intel Pentium 4. Conformational search of the macrocyclic molecule (***R***)-$\mathbf{M^H}$ was carried out by Batchmin and Macromodel version 4.5 (Columbia University, NY) using the following options: MM2* Force Field, Montecarlo stochastic algorithm with 3000 generated structures, minimization by the Polak–Ribiere (PR) conjugate gradient. All the rotatable bonds were explored. The obtained geometries were analyzed by the homemade computer program C.A.T.[19–21] to exclude twin molecules and to make clusters based on energetic and geometric criteria. Structures of the B amines CH_3NH_2 and $(CH_3)_2NH$ were calculated optimizing their unique conformation by molecular mechanics using the MM2* Force Field, with PR conjugate gradient minimization. Docking simulations in vacuo were performed on the binary [(***R***)-$\mathbf{M^H}$·H·B]$^+$ adducts between the chiral macrocyclic hosts (***R***)-$\mathbf{M^H}$ (3 conformations within an energetic window of 4.5 kcal/mol) and the protonated amines CH_3NH_2 and $(CH_3)_2NH$ as guests (1 conformation), as well as on the three-body [$(($***R***)-$\mathbf{M^H})_2$·H·B]$^+$ and [(***R***)-$\mathbf{M^H}$·(***S***)-$\mathbf{M^H}$·H·B]$^+$ adducts considering the supramolecular species [(***R***)-$\mathbf{M^H}$·H·B]$^+$ as hosts (2 geometries for [(***R***)-$\mathbf{M^H}$·H·$(CH_3)_2NH$]$^+$ and 3 geometries for [(***R***)-$\mathbf{M^H}$·H·CH_3NH_2]$^+$) and either (***R***)-$\mathbf{M^H}$ or (***S***)-$\mathbf{M^H}$ as guest (3 conformers as above).

Dockings procedures were carried out in two steps:

1. multiconformational rigid docking performed on each couple of host and guest molecules using the MolInE program[19–21]. The host–guest approach options set were: 52 directions of translation and 272 relative orientations of guest to host for each couple of host–guest conformations;

2. selection performed on the ensemble of adducts obtained in the first step, using energetic and geometric criteria. The geometry of the so achieved complexes was optimized by full relaxing their structure using the Batchmin program with the following options set: MM2* Force Field, PR conjugate gradient minimization. All the conformer ensembles were analyzed by C.A.T. program to exclude twin molecules, make energetic clusters and perform calculations of Boltzmann populations.

Structures of the [$(($***R***)-$\mathbf{M^H})_2$·H·B]$^+$ and [(***R***)-$\mathbf{M^H}$·(***S***)-$\mathbf{M^H}$·H·B]$^+$ adducts and of the protonated [$(($***R***)-$\mathbf{M^H})_2$·H]$^+$ and [(***R***)-$\mathbf{M^H}$·(***S***)-$\mathbf{M^H}$·H]$^+$ dimers, obtained by removing the amine from the corresponding three-body complexes, were further optimized by the AM1

semiempirical method as implemented in the computer program SPARTAN 04 (Wavefunction, Inc., 18401 Von Karman Avenue, Suite 370 Irvine, CA 92612). This step was included to allow the free migration of the proton toward the most basic site within the complex: in all cases no proton migration was found from the amino group of B.

RESULTS AND DISCUSSION

CID of the proton-bound homochiral $[(\mathbf{M^X})_2\cdot H\cdot B]^+$ (X = H, D) complexes at 5–20 eV collision energies (lab frame) yields the corresponding $[(\mathbf{M^X})_2\cdot H]^+$, $[(\mathbf{M^X}\cdot H\cdot B]^+$, and $[\mathbf{M^X}\cdot H]^+$ fragments (Scheme 1). Under the same conditions, the heterochiral $[\mathbf{M^H}\cdot\mathbf{M^D}\cdot H\cdot B]^+$ adducts yields the corresponding $[\mathbf{M^H}\cdot\mathbf{M^D}\cdot H]^+$, $[(\mathbf{M^X}\cdot H\cdot B]^+$, and $[\mathbf{M^X}\cdot H]^+$ fragments (Scheme 1). Their relative abundances are reported in Tables I–III, when B is CH_3NH_2, $(CH_3)_2NH$, and (*S*)-(–)-1-phenylethylamine, respectively. As pointed out above, the comparison of the CID spectra of the proton-bound homochiral $[(\mathbf{M^X})_2\cdot H\cdot B]^+$ (X = H, D) complexes provides an estimate of the overall isotope effect on the fragmentation process. Such a comparison is illustrated in Figs 1–3 for $\mathbf{M^X}$ = (***R***)-$\mathbf{M^H}$ or (***S***)-$\mathbf{M^D}$. Similar plots have been obtained for the homochiral complexes with $\mathbf{M^X}$ = (***S***)-$\mathbf{M^H}$ or (***R***)-$\mathbf{M^D}$ (Figs S1–S3 in Supporting Information). In all instances, it is observed that all $[(\mathbf{M^X})_2\cdot H]^+$ vs $[\mathbf{M^X}\cdot H]^+$ (X = H, D) points tend to follow the same linear correlation (circles in Figs 1–3). The same is observed as regards to all the $[(\mathbf{M^X}\cdot H\cdot B]^+$ vs $[\mathbf{M^X}\cdot H]^+$ (X = H, D) ones (squares in Figs 1–3). This coincidence excludes any significant effect of H/D substitution at the methoxy groups of the tetra-amide macrocycles of Chart 1 on the CID of the homochiral $[(\mathbf{M^X})_2\cdot H\cdot B]^+$ complexes within the range of collision energies (E_{lab} = 5–20 eV) delimited by the broken arrows in the Figures. Furthermore, the very similar abundances of the $[\mathbf{M^H}\cdot H\cdot B]^+$ and $[\mathbf{M^D}\cdot H\cdot B]^+$ fragments (Fig. 4) and of the $[\mathbf{M^H}\cdot H]^+$ and $[\mathbf{M^D}\cdot H]^+$ ones

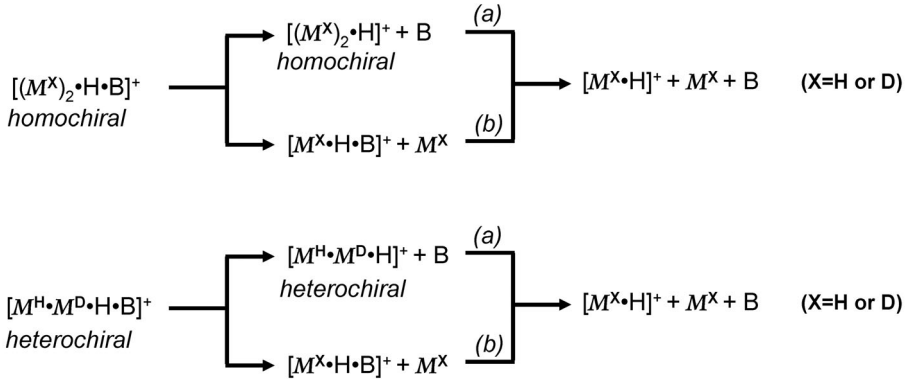

SCHEME 1

TABLE I
CID spectra of the homochiral $[(\mathbf{M}^{\mathbf{X}})_2 \cdot \mathrm{H} \cdot \mathrm{B}]^+$ (X = H, D) and the heterochiral $[\mathbf{M}^{\mathbf{H}} \cdot \mathbf{M}^{\mathbf{D}} \cdot \mathrm{H} \cdot \mathrm{B}]^+$ complexes

Mixture	E_{lab} eV	Ion relative abundance, %					
$\mathbf{M}^{\mathbf{H}}$ = (*R*)-$\mathbf{M}^{\mathbf{H}}$ $\mathbf{M}^{\mathbf{D}}$ = (*S*)-$\mathbf{M}^{\mathbf{D}}$ B = CH_3NH_2		$[(\mathbf{M}^{\mathbf{H}})_2 \cdot \mathrm{H} \cdot \mathrm{B}]^+$	$[(\mathbf{M}^{\mathbf{H}})_2 \cdot \mathrm{H}]^+$	$[\mathbf{M}^{\mathbf{H}} \cdot \mathrm{H} \cdot \mathrm{B}]^+$		$[\mathbf{M}^{\mathbf{H}} \cdot \mathrm{H}]^+$	
	5	55.1	33.8	0.2		10.9	
	10	39.9	29.9	1.1		29.1	
	15	14.9	23.7	1.9		59.5	
	20	5.5	15.2	2.2		77.1	
		$[(\mathbf{M}^{\mathbf{D}})_2 \cdot \mathrm{H} \cdot \mathrm{B}]^+$	$[(\mathbf{M}^{\mathbf{D}})_2 \cdot \mathrm{H}]^+$	$[\mathbf{M}^{\mathbf{D}} \cdot \mathrm{H} \cdot \mathrm{B}]^+$		$[\mathbf{M}^{\mathbf{D}} \cdot \mathrm{H}]^+$	
	5	63.1	25.1	0.7		11.1	
	10	47.5	27.8	0.9		23.9	
	15	22.3	23.8	2.1		51.8	
	20	5.9	15.5	2.7		75.9	
		$[\mathbf{M}^{\mathbf{H}} \cdot \mathbf{M}^{\mathbf{D}} \cdot \mathrm{H} \cdot \mathrm{B}]^+$	$[\mathbf{M}^{\mathbf{H}} \cdot \mathbf{M}^{\mathbf{D}} \cdot \mathrm{H}]^+$	$[\mathbf{M}^{\mathbf{H}} \cdot \mathrm{H} \cdot \mathrm{B}]^+$	$[\mathbf{M}^{\mathbf{D}} \cdot \mathrm{H} \cdot \mathrm{B}]^+$	$[\mathbf{M}^{\mathbf{H}} \cdot \mathrm{H}]^+$	$[\mathbf{M}^{\mathbf{D}} \cdot \mathrm{H}]^+$
	5	24.3	70.5	0.1	0.2	3.2	1.7
	10	15.1	70.4	0.3	0.2	7.4	6.6
	15	4.7	56.9	0.4	0.4	17.5	20.1
	20	1.6	33.8	0.7	0.6	31.4	32.0
$\mathbf{M}^{\mathbf{H}}$ = (*S*)-$\mathbf{M}^{\mathbf{H}}$ $\mathbf{M}^{\mathbf{D}}$ = (*R*)-$\mathbf{M}^{\mathbf{D}}$ B = CH_3NH_2		$[(\mathbf{M}^{\mathbf{H}})_2 \cdot \mathrm{H} \cdot \mathrm{B}]^+$	$[(\mathbf{M}^{\mathbf{H}})_2 \cdot \mathrm{H}]^+$	$[\mathbf{M}^{\mathbf{H}} \cdot \mathrm{H} \cdot \mathrm{B}]^+$		$[\mathbf{M}^{\mathbf{H}} \cdot \mathrm{H}]^+$	
	5	60.7	30.9	0.4		8.0	
	10	43.8	38.0	0.7		17.6	
	15	24.7	32.9	1.4		41.0	
	20	6.4	22.8	2.0		68.9	
		$[(\mathbf{M}^{\mathbf{D}})_2 \cdot \mathrm{H} \cdot \mathrm{B}]^+$	$[(\mathbf{M}^{\mathbf{D}})_2 \cdot \mathrm{H}]^+$	$[\mathbf{M}^{\mathbf{D}} \cdot \mathrm{H} \cdot \mathrm{B}]^+$		$[\mathbf{M}^{\mathbf{D}} \cdot \mathrm{H}]^+$	
	5	55.3	27.7	0.9		16.0	
	10	38.5	28.9	1.4		31.1	
	15	21.5	21.7	1.4		55.4	
	20	7.4	12.3	2.2		78.1	
		$[\mathbf{M}^{\mathbf{H}} \cdot \mathbf{M}^{\mathbf{D}} \cdot \mathrm{H} \cdot \mathrm{B}]^+$	$[\mathbf{M}^{\mathbf{H}} \cdot \mathbf{M}^{\mathbf{D}} \cdot \mathrm{H}]^+$	$[\mathbf{M}^{\mathbf{H}} \cdot \mathrm{H} \cdot \mathrm{B}]^+$	$[\mathbf{M}^{\mathbf{D}} \cdot \mathrm{H} \cdot \mathrm{B}]^+$	$[\mathbf{M}^{\mathbf{H}} \cdot \mathrm{H}]^+$	$[\mathbf{M}^{\mathbf{D}} \cdot \mathrm{H}]^+$
	5	24.1	68.5	0.1	0.2	3.4	3.7
	10	15.2	70.4	0.3	0.2	7.2	6.7
	15	11.5	40.0	0.5	0.8	24.1	23.1
	20	2.4	31.3	0.9	0.7	30.0	34.7

TABLE II

CID spectra of the homochiral $[(\mathbf{M}^{\mathbf{X}})_2 \cdot H \cdot B]^+$ (X = H, D) and the heterochiral $[\mathbf{M}^{\mathbf{H}} \cdot \mathbf{M}^{\mathbf{D}} \cdot H \cdot B]^+$ complexes

Mixture	E_{lab} eV	Ion relative abundance, %					
$\mathbf{M}^{\mathbf{H}}$ = (*R*)-$\mathbf{M}^{\mathbf{H}}$ $\mathbf{M}^{\mathbf{D}}$ = (*S*)-$\mathbf{M}^{\mathbf{D}}$ B = $(CH_3)_2NH$		$[(\mathbf{M}^{\mathbf{H}})_2 \cdot H \cdot B]^+$	$[(\mathbf{M}^{\mathbf{H}})_2 \cdot H]^+$	$[\mathbf{M}^{\mathbf{H}} \cdot H \cdot B]^+$		$[\mathbf{M}^{\mathbf{H}} \cdot H]^+$	
	5	71.3	2.0	12.7		14.0	
	10	50.4	1.8	22.4		25.4	
	15	18.9	1.2	34.7		45.2	
	20	6.5	0.6	34.1		58.8	
		$[(\mathbf{M}^{\mathbf{D}})_2 \cdot H \cdot B]^+$	$[(\mathbf{M}^{\mathbf{D}})_2 \cdot H]^+$	$[\mathbf{M}^{\mathbf{D}} \cdot H \cdot B]^+$		$[\mathbf{M}^{\mathbf{D}} \cdot H]^+$	
	5	64.1	1.8	15.8		18.3	
	10	45.4	2.2	24.6		27.8	
	15	18.1	1.2	36.6		44.1	
	20	5.9	0.5	39.7		53.9	
		$[\mathbf{M}^{\mathbf{H}} \cdot \mathbf{M}^{\mathbf{D}} \cdot H \cdot B]^+$	$[\mathbf{M}^{\mathbf{H}} \cdot \mathbf{M}^{\mathbf{D}} \cdot H]^+$	$[\mathbf{M}^{\mathbf{H}} \cdot H \cdot B]^+$	$[\mathbf{M}^{\mathbf{D}} \cdot H \cdot B]^+$	$[\mathbf{M}^{\mathbf{H}} \cdot H]^+$	$[\mathbf{M}^{\mathbf{D}} \cdot H]^+$
	5	56.4	11.5	7.2	8.4	8.2	8.2
	10	33.9	9.3	15.3	13.9	11.5	16.2
	15	11.9	4.6	18.1	19.9	24.1	21.3
	20	3.8	2.0	20.1	19.9	29.8	24.4
$\mathbf{M}^{\mathbf{H}}$ = (*S*)-$\mathbf{M}^{\mathbf{H}}$ $\mathbf{M}^{\mathbf{D}}$ = (*R*)-$\mathbf{M}^{\mathbf{D}}$ B = $(CH_3)_2NH$		$[(\mathbf{M}^{\mathbf{H}})_2 \cdot H \cdot B]^+$	$[(\mathbf{M}^{\mathbf{H}})_2 \cdot H]^+$	$[\mathbf{M}^{\mathbf{H}} \cdot H \cdot B]^+$		$[\mathbf{M}^{\mathbf{H}} \cdot H]^+$	
	5	73.9	1.9	12.6		11.6	
	10	47.6	1.5	25.0		25.9	
	15	22.1	0.8	32.5		44.6	
	20	7.0	0.2	39.1		53.7	
		$[(\mathbf{M}^{\mathbf{D}})_2 \cdot H \cdot B]^+$	$[(\mathbf{M}^{\mathbf{D}})_2 \cdot H]^+$	$[\mathbf{M}^{\mathbf{D}} \cdot H \cdot B]^+$		$[\mathbf{M}^{\mathbf{D}} \cdot H]^+$	
	5	72.3	1.7	11.9		14.1	
	10	44.8	2.2	24.3		28.7	
	15	18.7	1.0	39.7		40.6	
	20	5.6	0.5	41.1		52.8	
		$[\mathbf{M}^{\mathbf{H}} \cdot \mathbf{M}^{\mathbf{D}} \cdot H \cdot B]^+$	$[\mathbf{M}^{\mathbf{H}} \cdot \mathbf{M}^{\mathbf{D}} \cdot H]^+$	$[\mathbf{M}^{\mathbf{H}} \cdot H \cdot B]^+$	$[\mathbf{M}^{\mathbf{D}} \cdot H \cdot B]^+$	$[\mathbf{M}^{\mathbf{H}} \cdot H]^+$	$[\mathbf{M}^{\mathbf{D}} \cdot H]^+$
	5	62.7	8.9	7.9	5.6	7.3	7.7
	10	35.7	7.9	13.8	13.6	13.0	14.2
	15	16.5	4.1	17.5	19.5	22.1	20.2
	20	4.1	2.2	19.7	19.0	27.7	27.2

TABLE III
CID spectra of the homochiral $[(\mathbf{M}^{\mathbf{X}})_2 \cdot \mathrm{H} \cdot \mathrm{B}]^+$ (X = H, D) and the heterochiral $[\mathbf{M}^{\mathbf{H}} \cdot \mathbf{M}^{\mathbf{D}} \cdot \mathrm{H} \cdot \mathrm{B}]^+$ complexes

Mixture	E_{lab} eV	Ion relative abundance, %					
$\mathbf{M}^{\mathbf{H}}$ = (*R*)-$\mathbf{M}^{\mathbf{H}}$ $\mathbf{M}^{\mathbf{D}}$ = (*S*)-$\mathbf{M}^{\mathbf{D}}$ B = (*S*)-$PhCHCH_3NH_2$		$[(\mathbf{M}^{\mathbf{H}})_2 \cdot \mathrm{H} \cdot \mathrm{B}]^+$	$[(\mathbf{M}^{\mathbf{H}})_2 \cdot \mathrm{H}]^+$	$[\mathbf{M}^{\mathbf{H}} \cdot \mathrm{H} \cdot \mathrm{B}]^+$		$[\mathbf{M}^{\mathbf{H}} \cdot \mathrm{H}]^+$	
	5	57.8	12.1	7.2		22.9	
	10	45.5	13.8	8.5		32.1	
	15	18.8	6.7	13.4		61.2	
	20	9.2	6.4	17.6		66.8	
		$[(\mathbf{M}^{\mathbf{D}})_2 \cdot \mathrm{H} \cdot \mathrm{B}]^+$	$[(\mathbf{M}^{\mathbf{D}})_2 \cdot \mathrm{H}]^+$	$[\mathbf{M}^{\mathbf{D}} \cdot \mathrm{H} \cdot \mathrm{B}]^+$		$[\mathbf{M}^{\mathbf{D}} \cdot \mathrm{H}]^+$	
	5	56.8	15.4	7.8		20.0	
	10	40.1	14.7	10.4		34.8	
	15	21.3	8.8	13.1		56.7	
	20	5.5	4.2	13.8		76.5	
		$[\mathbf{M}^{\mathbf{H}} \cdot \mathbf{M}^{\mathbf{D}} \cdot \mathrm{H} \cdot \mathrm{B}]^+$	$[\mathbf{M}^{\mathbf{H}} \cdot \mathbf{M}^{\mathbf{D}} \cdot \mathrm{H}]^+$	$[\mathbf{M}^{\mathbf{H}} \cdot \mathrm{H} \cdot \mathrm{B}]^+$	$[\mathbf{M}^{\mathbf{D}} \cdot \mathrm{H} \cdot \mathrm{B}]^+$	$[\mathbf{M}^{\mathbf{H}} \cdot \mathrm{H}]^+$	$[\mathbf{M}^{\mathbf{D}} \cdot \mathrm{H}]^+$
	5	37.6	49.6	2.5	2.4	4.1	3.9
	10	24.5	53.0	4.3	2.7	9.3	6.2
	15	13.2	23.6	6.0	5.8	23.7	27.8
	20	3.5	15.3	8.1	6.4	35.7	31.0
$\mathbf{M}^{\mathbf{H}}$ = (*S*)-$\mathbf{M}^{\mathbf{H}}$ $\mathbf{M}^{\mathbf{D}}$ = (*R*)-$\mathbf{M}^{\mathbf{D}}$ B = (*S*)-$PhCHCH_3NH_2$		$[(\mathbf{M}^{\mathbf{H}})_2 \cdot \mathrm{H} \cdot \mathrm{B}]^+$	$[(\mathbf{M}^{\mathbf{H}})_2 \cdot \mathrm{H}]^+$	$[\mathbf{M}^{\mathbf{H}} \cdot \mathrm{H} \cdot \mathrm{B}]^+$		$[\mathbf{M}^{\mathbf{H}} \cdot \mathrm{H}]^+$	
	5	66.7	11.6	4.6		17.1	
	10	40.8	12.8	10.1		36.3	
	15	18.2	6.7	14.3		60.7	
	20	6.2	5.1	14.2		74.6	
		$[(\mathbf{M}^{\mathbf{D}})_2 \cdot \mathrm{H} \cdot \mathrm{B}]^+$	$[(\mathbf{M}^{\mathbf{D}})_2 \cdot \mathrm{H}]^+$	$[\mathbf{M}^{\mathbf{D}} \cdot \mathrm{H} \cdot \mathrm{B}]^+$		$[\mathbf{M}^{\mathbf{D}} \cdot \mathrm{H}]^+$	
	5	64.4	11.7	5.2		18.7	
	10	42.4	10.7	11.4		35.6	
	15	15.8	10.0	15.9		58.2	
	20	4.1	3.9	15.6		76.3	
		$[\mathbf{M}^{\mathbf{H}} \cdot \mathbf{M}^{\mathbf{D}} \cdot \mathrm{H} \cdot \mathrm{B}]^+$	$[\mathbf{M}^{\mathbf{H}} \cdot \mathbf{M}^{\mathbf{D}} \cdot \mathrm{H}]^+$	$[\mathbf{M}^{\mathbf{H}} \cdot \mathrm{H} \cdot \mathrm{B}]^+$	$[\mathbf{M}^{\mathbf{D}} \cdot \mathrm{H} \cdot \mathrm{B}]^+$	$[\mathbf{M}^{\mathbf{H}} \cdot \mathrm{H}]^+$	$[\mathbf{M}^{\mathbf{D}} \cdot \mathrm{H}]^+$
	5	38.3	44.5	2.1	1.7	6.5	6.8
	10	30.5	33.4	4.1	4.5	15.1	12.5
	15	11.7	24.3	5.5	6.2	23.3	29.0
	20	3.4	16.3	7.9	6.7	32.0	33.7

(Fig. 5) from CID of $[\mathbf{M^H{\cdot}M^D{\cdot}}H{\cdot}B]^+$ excludes any significant isotope effect on their formation.

The ca. –1 slope of the linear inverse $[(\mathbf{M^X})_2{\cdot}H]^+$ vs $[\mathbf{M^X{\cdot}}H]^+$ (X = H, D) correlations (circles in Figs 1 and S1), observed with B = CH_3NH_2, suggests a strict parent/daughter relationship between the two fragments. This means that $[\mathbf{M^X{\cdot}}H]^+$ arises almost exclusively from further fragmentation of $[(\mathbf{M^X})_2{\cdot}H]^+$ (path (*a*) in Scheme 1). This conclusion is corroborated by the absence of any inverse $[\mathbf{M^X{\cdot}}H{\cdot}B]^+$ vs $[\mathbf{M^X{\cdot}}H]^+$ correlation under the same conditions (squares in Figs 1 and S1).

A similar picture is observed with regards to the fragmentation pattern from CID of $[(\mathbf{M^X})_2{\cdot}H{\cdot}B]^+$ (B = (*S*)-(–)-1-phenylethylamine). Indeed, the –1 slope of the linear inverse $[(\mathbf{M^X})_2{\cdot}H]^+$ vs $[\mathbf{M^X{\cdot}}H]^+$ correlation (circles in Figs 3 and S3) suggests that $[\mathbf{M^X{\cdot}}H]^+$ arises predominantly from further fragmentation of $[(\mathbf{M^X})_2{\cdot}H]^+$. No significant contribution of $[\mathbf{M^X{\cdot}}H{\cdot}B]^+$ to $[\mathbf{M^X{\cdot}}H]^+$ is

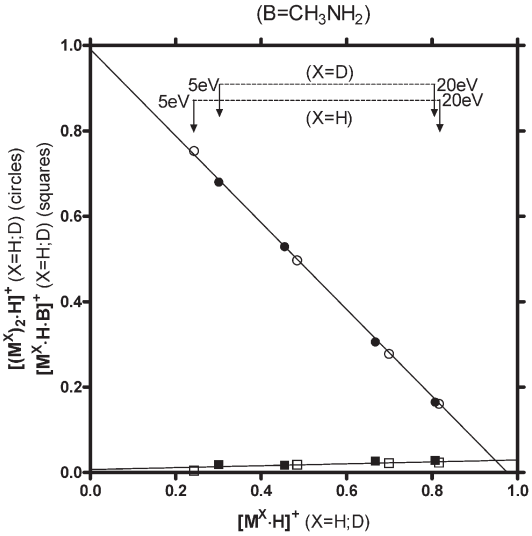

FIG. 1

Comparative plots of the relative abundances of the products from CID of the homochiral $[(\mathbf{M^X})_2{\cdot}H{\cdot}B]^+$ (X = H, D) complexes from ESI of the (***R***)-$\mathbf{M^H}$/(***S***)-$\mathbf{M^D}$/B = CH_3NH_2 mixture: open circles $[((\boldsymbol{R})\text{-}\mathbf{M^H})_2{\cdot}H]^+$ vs $[(\boldsymbol{R})\text{-}\mathbf{M^H}{\cdot}H]^+$, full circles $[((\boldsymbol{S})\text{-}\mathbf{M^D})_2{\cdot}H]^+$ vs $[(\boldsymbol{S})\text{-}\mathbf{M^D}{\cdot}H]^+$, open squares $[(\boldsymbol{R})\text{-}\mathbf{M^H}{\cdot}H{\cdot}B]^+$ vs $[(\boldsymbol{R})\text{-}\mathbf{M^H}{\cdot}H]^+$, full squares $[(\boldsymbol{S})\text{-}\mathbf{M^D}{\cdot}H{\cdot}B]^+$ vs $[(\boldsymbol{S})\text{-}\mathbf{M^D}{\cdot}H]^+$. The upper broken arrows denote the collision energy (E_{lab}) range for $[((\boldsymbol{R})\text{-}\mathbf{M^H})_2{\cdot}H{\cdot}B]^+$ and the lower ones that for $[((\boldsymbol{S})\text{-}\mathbf{M^D})_2{\cdot}H{\cdot}B]^+$ (see Table I)

detectable in these systems, as demonstrated by the essential constancy of its relative abundance at all collision energies (squares in Figs 3 and S3).

A rather different picture is observed in the CID of $[(\mathbf{M^X})_2\cdot\mathrm{H}\cdot\mathrm{B}]^+$ (B = $(CH_3)_2NH$). Here, two linear inverse $[\mathbf{M^X}\cdot\mathrm{H}\cdot\mathrm{B}]^+$ vs $[\mathbf{M^X}\cdot\mathrm{H}]^+$ (squares in Figs 2 and S2) and $[(\mathbf{M^X})_2\cdot\mathrm{H}]^+$ vs $[\mathbf{M^X}\cdot\mathrm{H}]^+$ correlation curves (circles in Figs 2 and S2) are observed whose slopes (ca. 0.5) suggest that, in this case, both $[(\mathbf{M^X})_2\cdot\mathrm{H}]^+$ and $[\mathbf{M^X}\cdot\mathrm{H}\cdot\mathrm{B}]^+$ undergo fragmentation to give $[\mathbf{M^X}\cdot\mathrm{H}]^+$ in proportions corresponding approximately to their abundance (paths (*a*) and (*b*) of Scheme 1).

The linear correlations of Figs 1–3 and S1–S3 are redrawn as broken lines in Figs 6–8, respectively, together with $[\mathbf{M^X}\cdot\mathrm{H}\cdot\mathrm{B}]^+$ vs $[\mathbf{M^X}\cdot\mathrm{H}]^+$ (squares) and $[\mathbf{M^H}\cdot\mathbf{M^D}\cdot\mathrm{H}]^+$ vs $[\mathbf{M^X}\cdot\mathrm{H}]^+$ points (circles) measured from the CID of the heterochiral $[\mathbf{M^H}\cdot\mathbf{M^D}\cdot\mathrm{H}\cdot\mathrm{B}]^+$ complexes. A first point to be considered is the fact that, within the same collision energy range E_{lab} = 5–20 eV (delim-

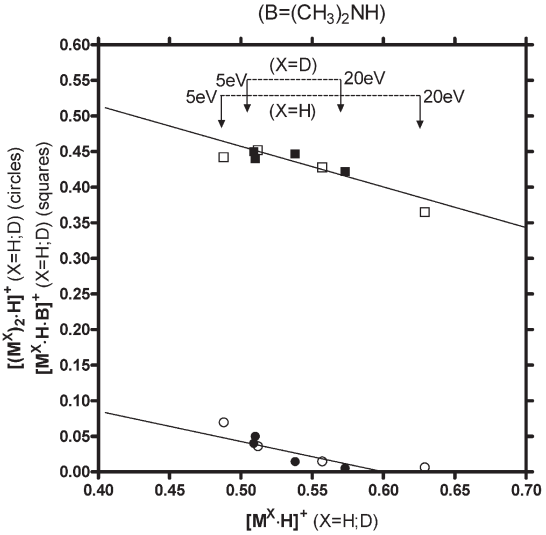

FIG. 2

Comparative plots of the relative abundances of the products from CID of the homochiral $[(\mathbf{M^X})_2\cdot\mathrm{H}\cdot\mathrm{B}]^+$ (X = H, D) complexes from ESI of the (***R***)-$\mathbf{M^H}$/(***S***)-$\mathbf{M^D}$/B = $(CH_3)_2NH$ mixture: open circles $[((\boldsymbol{R})\text{-}\mathbf{M^H})_2\cdot\mathrm{H}]^+$ vs $[(\boldsymbol{R})\text{-}\mathbf{M^H}\cdot\mathrm{H}]^+$, full circles $[((\boldsymbol{S})\text{-}\mathbf{M^D})_2\cdot\mathrm{H}]^+$ vs $[(\boldsymbol{S})\text{-}\mathbf{M^D}\cdot\mathrm{H}]^+$, open squares, $[(\boldsymbol{R})\text{-}\mathbf{M^H}\cdot\mathrm{H}\cdot\mathrm{B}]^+$ vs $[(\boldsymbol{R})\text{-}\mathbf{M^H}\cdot\mathrm{H}]^+$, full squares $[(\boldsymbol{S})\text{-}\mathbf{M^D}\cdot\mathrm{H}\cdot\mathrm{B}]^+$ vs $[(\boldsymbol{S})\text{-}\mathbf{M^D}\cdot\mathrm{H}]^+$. The upper broken arrows denote the collision energy (E_{lab}) range for $[((\boldsymbol{R})\text{-}\mathbf{M^H})_2\cdot\mathrm{H}\cdot\mathrm{B}]^+$ and the lower ones that for $[((\boldsymbol{S})\text{-}\mathbf{M^D})_2\cdot\mathrm{H}\cdot\mathrm{B}]^+$ (see Table II)

ited in Figs 6–8 by the broken arrows), the extent of fragmentation of $[\mathbf{M^H{\cdot}M^D{\cdot}}H]^+$ and $[\mathbf{M^X{\cdot}}H{\cdot}B]^+$ to yield $[\mathbf{M^X{\cdot}}H]^+$ is significantly smaller with heterochiral $[\mathbf{M^H{\cdot}M^D{\cdot}}H{\cdot}B]^+$ complexes than the corresponding processes from the homochiral $[(\mathbf{M^X})_2{\cdot}H{\cdot}B]^+$ ones (whose E_{lab} = 5–20 eV range corresponds in Figs 6–8 to the shadowed areas). Furthermore, a large deviation from the linear curves is observed with $[\mathbf{M^H{\cdot}M^D{\cdot}}H{\cdot}B]^+$ (B = $(CH_3)_2NH$) (Fig. 7), especially at the lowest collision energies, where the relative abundances of the $[\mathbf{M^H{\cdot}M^D{\cdot}}H]^+$ and $[\mathbf{M^X{\cdot}}H{\cdot}B]^+$ fragments tend to merge. This behaviour is indicative of the fact that, at low internal energies, the heterochiral $[\mathbf{M^H{\cdot}M^D{\cdot}}H{\cdot}B]^+$ (B = $(CH_3)_2NH$) complexes tend to release more B than $\mathbf{M^X}$ (X = H, D), relative to their homochiral counterparts[22]. Furthermore, the non-linearity of the experimental points of Fig. 7 is suggestive of a pronounced internal energy effect in the competing (*a*) and (*b*) fragmentations of the heterochiral complexes relative to the homochiral ones

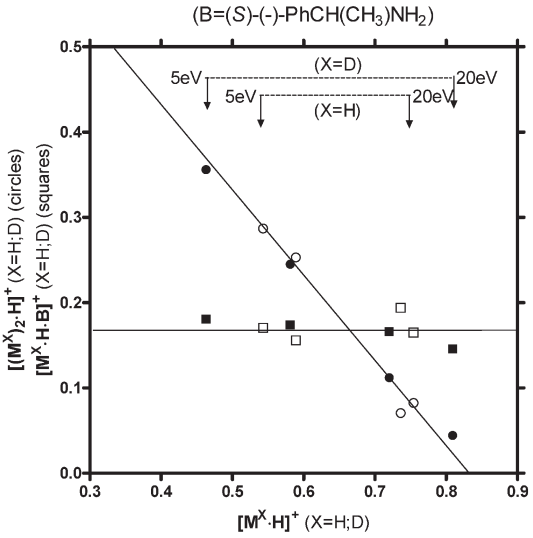

FIG. 3

Comparative plots of the relative abundances of the products from CID of the homochiral $[(\mathbf{M^X})_2{\cdot}H{\cdot}B]^+$ (X = H, D) complexes from ESI of the (***R***)-$\mathbf{M^H}$/(***S***)-$\mathbf{M^D}$/B = (*S*)-(–)-1-phenylethylamine mixture: open circles $[((\boldsymbol{R})\text{-}\mathbf{M^H})_2{\cdot}H]^+$ vs $[(\boldsymbol{R})\text{-}\mathbf{M^H{\cdot}}H]^+$, full circles $[((\boldsymbol{S})\text{-}\mathbf{M^D})_2{\cdot}H]^+$ vs $[(\boldsymbol{S})\text{-}\mathbf{M^D{\cdot}}H]^+$, open squares $[(\boldsymbol{R})\text{-}\mathbf{M^H{\cdot}}H{\cdot}B]^+$ vs $[(\boldsymbol{R})\text{-}\mathbf{M^H{\cdot}}H]^+$, full squares $[(\boldsymbol{S})\text{-}\mathbf{M^D{\cdot}}H{\cdot}B]^+$ vs $[(\boldsymbol{S})\text{-}\mathbf{M^D{\cdot}}H]^+$. The upper broken arrows denote the collision energy (E_{lab}) range for $[((\boldsymbol{R})\text{-}\mathbf{M^H})_2{\cdot}H{\cdot}B]^+$ and the lower ones that for $[((\boldsymbol{S})\text{-}\mathbf{M^D})_2{\cdot}H{\cdot}B]^+$ (see Table III)

(Scheme 1). No significant deviations from linearity are instead observed in the CID of $[\mathbf{M^H{\cdot}M^D{\cdot}}H{\cdot}B]^+$ (B = CH_3NH_2, (*S*)-(–)-1-phenylethylamine) (Figs 6 and 8, respectively) which suggest that, in these cases, the excitation energy dependence of the fragmentation paths (*a*) and (*b*) is the same in both the hetero- and the homochiral complexes. Besides, the almost perfect alignment of the experimental points in Fig. 8 excludes any significant effects of the configuration of the chiral amine B on the fragmentation pattern.

In order to gain a better understanding of the factors determining the different CID patterns of the homochiral $[(\mathbf{M^X})_2{\cdot}H{\cdot}B]^+$ and the heterochiral $[\mathbf{M^H{\cdot}M^D{\cdot}}H{\cdot}B]^+$ complexes, we have performed a theoretical investigation based on molecular modeling calculations. Owing to the quite large size, flexibility, and complexity of the isolated hosts and their adducts, a reasonably complete and homogeneous sampling of the potential energy hypersurfaces related to the conformational variability of the single species and to the intermolecular host–guest interactions can only be obtained using computationally non-demanding methods. Our approach uses molecular

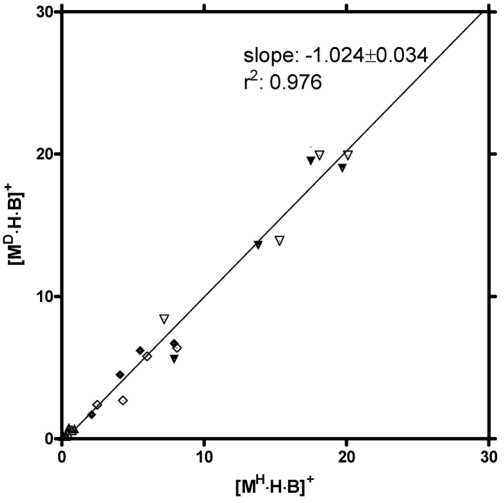

FIG. 4
Comparative plots of the relative abundances of the $[\mathbf{M^H{\cdot}}H{\cdot}B]^+$ and $[\mathbf{M^D{\cdot}}H{\cdot}B]^+$ fragments from CID of the heterochiral $[\mathbf{M^H{\cdot}M^D{\cdot}}H{\cdot}B]^+$ complexes ($\mathbf{M^H}/\mathbf{M^D}$ = ($\boldsymbol{R}$)-$\mathbf{M^H}$/($\boldsymbol{S}$)-$\mathbf{M^D}$ (open symbols), ($\boldsymbol{S}$)-$\mathbf{M^H}$/($\boldsymbol{R}$)-$\mathbf{M^D}$ (full symbols); B = CH_3NH_2 (triangles), $(CH_3)_2NH$ (reverse triangles), and (*S*)-(–)-α-methylbenzylamine (diamonds)) (see Tables I–III)

mechanic models that are computationally light and provide an excellent account of conformational energy differences for organic compounds. Preliminary exhaustive conformational searches and relevant analyses have been first carried out on structures of macrocycles (***R***)-$\mathbf{M^H}$ by means of molecular mechanics using the MM2* force field (see Experimental). Structures of guests B = CH_3NH_2 and $(CH_3)_2NH$ in their protonated form were calculated by simply optimization of their unique conformation at the same level of theory. Three geometries among the more stable conformers of (***R***)-$\mathbf{M^H}$ (and of (***S***)-$\mathbf{M^H}$ as well), i.e. *eq-eq*, *ax-ax*, and *ax-eq* (Chart 2), have been selected within an energy window of 4.5 kcal/mol as the representative ensemble of its structure. Such geometries were employed to perform multiconformational molecular docking simulations of $[(\boldsymbol{R})\text{-}\mathbf{M^H}\cdot H\cdot B]^+$ and $[(\boldsymbol{S})\text{-}\mathbf{M^H}\cdot H\cdot B]^+$ adducts by interaction of $[(\boldsymbol{R})\text{-}\mathbf{M^H}\cdot H]^+$ and $[(\boldsymbol{S})\text{-}\mathbf{M^H}\cdot H]^+$ with guests B. Simulated complexes were represented by ensembles of adducts, selected by geometric and energetic criteria to afford two geometries for $[(\boldsymbol{R})\text{-}\mathbf{M^H}\cdot H\cdot(CH_3)_2NH]^+$ (and $[(\boldsymbol{S})\text{-}\mathbf{M^H}\cdot H\cdot(CH_3)_2NH]^+$) and three for

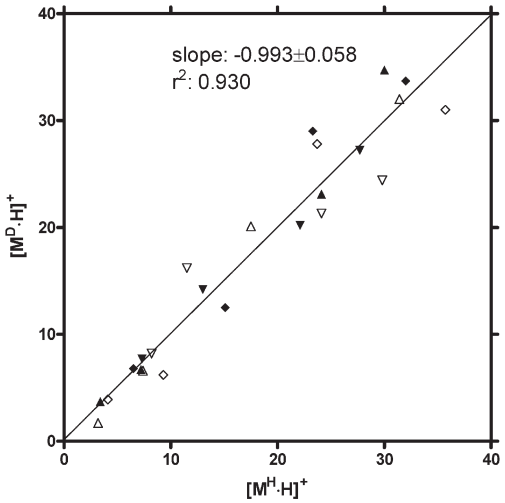

FIG. 5

Comparative plots of the relative abundances of the $[\mathbf{M^H}\cdot H]^+$ and $[\mathbf{M^D}\cdot H]^+$ fragments from CID of the heterochiral $[\mathbf{M^H}\cdot\mathbf{M^D}\cdot H\cdot B]^+$ complexes ($\mathbf{M^H}/\mathbf{M^D}$ = (***R***)-$\mathbf{M^H}$/(***S***)-$\mathbf{M^D}$ (open symbols), (***S***)-$\mathbf{M^H}$/(***R***)-$\mathbf{M^D}$ (full symbols); B = CH_3NH_2 (triangles), $(CH_3)_2NH$ (reverse triangles), and (*S*)-(–)-α-methylbenzylamine (diamonds)) (see Tables I–III)

[(***R***)-$\mathbf{M^H}$·H·CH_3NH_2]$^+$ (and [(***S***)-$\mathbf{M^H}$·H·CH_3NH_2]$^+$). Similarly to results already obtained by docking simulations between (***R***)-$\mathbf{M^H}$ and amino acid derivatives[8], we found that complexation of the guest induces a conformational change of the host, from the largely populated *eq-eq* form present in the free species (98.4% Boltzmann population) to the prevalent *ax-ax* conformation, irrespective of the nature of the guest B (54.4% within [(***R***)-$\mathbf{M^H}$·H·CH_3NH_2]$^+$ and 85.5% within [(***R***)-$\mathbf{M^H}$·H·$(CH_3)_2NH$]$^+$. These binary adducts were in turn employed as hosts in new multiconformational docking experiments using either (***R***)-$\mathbf{M^H}$ or (***S***)-$\mathbf{M^H}$ as guests, to afford the proton-bound three-body homo- [((***R***)-$\mathbf{M^H}$)$_2$·H·B]$^+$ and heterochiral [(***R***)-$\mathbf{M^H}$·(***S***)-$\mathbf{M^H}$·H·B]$^+$ complexes, respectively. To describe the macroscopic geometry and stability of the complexes as average properties, the adducts have been again represented by ensembles of the lower energy geometries within a 3 kcal/mol window. All the final structures were then further opti-

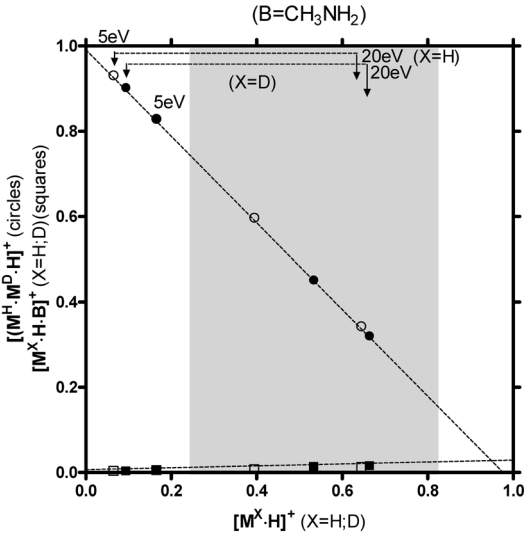

FIG. 6

Comparative plots of [$\mathbf{M^X}$·H·B]$^+$ vs [$\mathbf{M^X}$·H]$^+$ (X = H, D) (squares) and [$\mathbf{M^H}$·$\mathbf{M^D}$·H]$^+$ vs [$\mathbf{M^X}$·H]$^+$ (X = H, D) (circles) measured from the CID of the heterochiral [$\mathbf{M^H}$·$\mathbf{M^D}$·H·B]$^+$ (B = CH_3NH_2) complexes ($\mathbf{M^H}$/$\mathbf{M^D}$ = (***R***)-$\mathbf{M^H}$/(***S***)-$\mathbf{M^D}$ (open symbols), (***S***)-$\mathbf{M^H}$/(***R***)-$\mathbf{M^D}$ (full symbols)) (see Table I). The broken arrows refer to the corresponding collision energy (E_{lab}) range (Table I). The broken lines refer to the linear correlations of Fig. 1. The shadowed area refers to the collision energy (E_{lab}) ranges for the corresponding homochiral complexes (see Fig. 1)

mized by the AM1 semiempirical method, to allow the free proton migration toward the most basic site in the complex (either the carbonyl oxygens of the macrocycles or the amino group of B) from the initially imposed input protonation site (the amino group of B). After energy minimization, in all instances the proton was invariably found on the amino group of B, indicating that this is the most basic fragment within the complexes. Similarly to the induced fit already observed upon (***R***)-$\mathbf{M^H}$ vs B complexation, also in this case the interaction with the new guest (***R***)-$\mathbf{M^H}$ (or (***S***)-$\mathbf{M^H}$) promotes drastic conformational changes on the two macrocyclic units, that are found exclusively in the *eq-eq* geometries within all the three-body adducts.

The calculated structures of the homochiral $[((\boldsymbol{R})\text{-}\mathbf{M^H})_2 \cdot \mathrm{H} \cdot \mathrm{B}]^+$ complexes can be conveniently clustered in two, not too different in energy, ensembles (denoted as **I** and **II** in Fig. 9), according to the dispositions

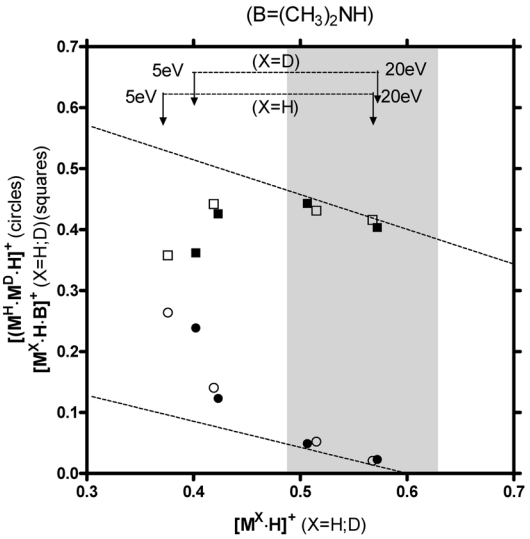

FIG. 7

Comparative plots of $[\mathbf{M^X}\cdot\mathrm{H}\cdot\mathrm{B}]^+$ vs $[\mathbf{M^X}\cdot\mathrm{H}]^+$ (X = H, D) (squares) and $[\mathbf{M^H}\cdot\mathbf{M^D}\cdot\mathrm{H}]^+$ vs $[\mathbf{M^X}\cdot\mathrm{H}]^+$ (X = H, D) (circles) measured from the CID of the heterochiral $[\mathbf{M^H}\cdot\mathbf{M^D}\cdot\mathrm{H}\cdot\mathrm{B}]^+$ (B = $(CH_3)_2NH$) complexes ($\mathbf{M^H}/\mathbf{M^D}$ = (***R***)-$\mathbf{M^H}$/(***S***)-$\mathbf{M^D}$ (open symbols), (***S***)-$\mathbf{M^H}$/(***R***)-$\mathbf{M^D}$ (full symbols)) (see Table II). The broken arrows refer to the corresponding collision energy (E_{lab}) range (Table II). The broken lines refer to the linear correlations of Fig. 2. The shadowed area refers to the collision energy (E_{lab}) ranges for the corresponding homochiral complexes (see Fig. 2)

assumed in each structure by the two host molecules, both in the *eq-eq* conformation. In contrast, the calculated geometries of the heterochiral $[(\boldsymbol{R})\text{-}\mathbf{M^H}\cdot(\boldsymbol{S})\text{-}\mathbf{M^H}\cdot H\cdot B]^+$ complex can be clustered in the single most stable ensemble (denoted as **III** in Fig. 9), where the two host molecules are again in the *eq-eq* conformation. As illustrated in Fig. 9, the homochiral structures **I** are characterized by several H-bonds among the ammonium hydrogens and the converging pair of carbonyls placed on the convex sides F2 of a first host molecule. The second host molecule interacts with the first one through a network of four H-bonds between the two couples of -CO-NH- groups placed on the outer margins of their concave sides F1. Within such a three-body complex the dimer $((\boldsymbol{R})\text{-}\mathbf{M^H})_2$ shows D_2 symmetry. Structures **I**, that remind two saddle roof faced on their concave sides, with the guest BH^+ interacting at the top of one of the two convex sides, will be hereafter

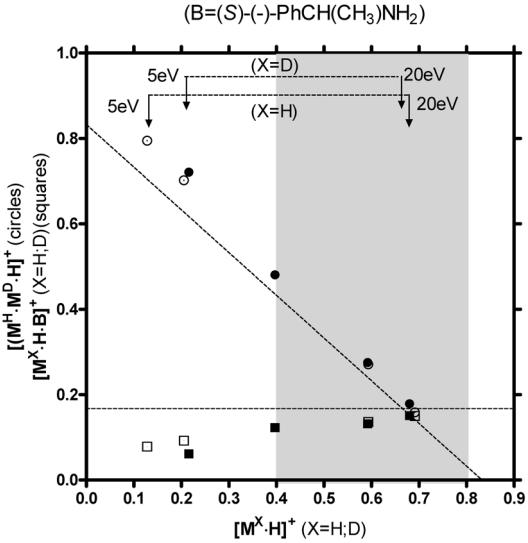

FIG. 8

Comparative plots of $[\mathbf{M^X}\cdot H\cdot B]^+$ vs $[\mathbf{M^X}\cdot H]^+$ (X = H, D) (squares) and $[M^{\mathbf{H}}\cdot M^{D}\cdot H]^+$ vs $[\mathbf{M^X}\cdot H]^+$ (X = H, D) (circles) measured from the CID of the heterochiral $[\mathbf{M^H}\cdot\mathbf{M^D}\cdot H\cdot B]^+$ (B = (*S*)-(–)-1-phenylethylamine) complexes ($\mathbf{M^H}/\mathbf{M^D}$ = $(\boldsymbol{R})\text{-}\mathbf{M^H}/(\boldsymbol{S})\text{-}\mathbf{M^D}$ (open symbols), $(\boldsymbol{S})\text{-}\mathbf{M^H}/(\boldsymbol{R})\text{-}\mathbf{M^D}$ (full symbols)) (see Table III). The broken arrows refer to the corresponding collision energy (E_{lab}) range (Table III). The broken lines refer to the linear correlations of Fig. 3. The shadowed area refers to the collision energy (E_{lab}) ranges for the corresponding homochiral complexes (see Fig. 3)

indicated by the symbol $\Diamond_{\mathbf{homo}}$. Their isomeric structures **II** are instead characterized by several H-bonds between the ammonium hydrogens and the converging pairs of carbonyls placed on the convex sides F2 of two facing host molecules. In this kind of complexes, the two macrocycles (***R***)-$\mathbf{M^H}$ assume a Y-shaped disposition and structures **II** will be hereafter indicated by the symbol $\mathbf{Y_{homo}}$. Finally, the heterochiral structures **III** show relative molecular disposition and H-bond network resembling those observed in $\mathbf{Y_{homo}}$ and, therefore, will be hereafter indicated by the symbol $\mathbf{Y_{hetero}}$.

Energy and typology of the simulated complexes $\Diamond_{\mathbf{homo}}$, $\mathbf{Y_{homo}}$ and $\mathbf{Y_{hetero}}$ can be conveniently analyzed to obtain a persuasive rationalization of the

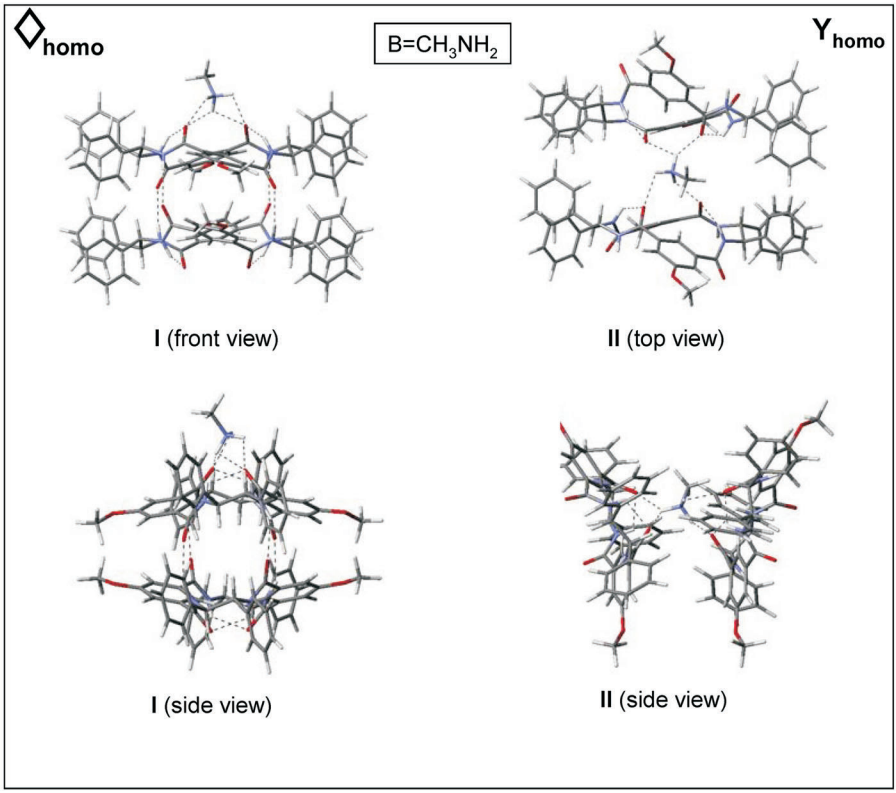

FIG. 9

Structures of global minima of the homochiral $[((\boldsymbol{R})\text{-}\mathbf{M^H})_2\cdot\mathrm{H}\cdot\mathrm{B}]^+$ and the heterochiral $[(\boldsymbol{R})\text{-}\mathbf{M^H}\cdot(\boldsymbol{S})\text{-}\mathbf{M^H}\cdot\mathrm{H}\cdot\mathrm{B}]^+$ complexes (B = CH_3NH_2 and $(CH_3)_2NH$)

corresponding experimental CID patterns. Inspection of Table I clearly shows that the privileged fragmentation path for both $[(\mathbf{M^X})_2{\cdot}H{\cdot}CH_3NH_2]^+$ and $[\mathbf{M^H}{\cdot}\mathbf{M^D}{\cdot}H{\cdot}CH_3NH_2]^+$ adducts is represented by loss of CH_3NH_2. On the contrary, the favoured fragmentation path for both $[(\mathbf{M^X})_2{\cdot}H{\cdot}(CH_3)_2NH]^+$ and $[\mathbf{M^H}{\cdot}\mathbf{M^D}{\cdot}H{\cdot}(CH_3)_2NH]^+$ is the release of a host molecule (Table II). Calculations on $[((\boldsymbol{R})\text{-}\mathbf{M^H})_2{\cdot}H{\cdot}CH_3NH_2]^+$ indicated that the $\mathbf{Y_{homo}}$ geometry is the most stable one, corresponding to a Boltzmann population of 90%. This is the same kind of geometry found for the heterochiral $[(\boldsymbol{R})\text{-}\mathbf{M^H}{\cdot}(\boldsymbol{S})\text{-}\mathbf{M^H}{\cdot}H{\cdot}CH_3NH_2]^+$ complex, whose $\mathbf{Y_{hetero}}$ structure is even lower in energy by about 0.8 kcal/mol. Interestingly, calculations also indicated that the protonated heterodimer $[(\boldsymbol{R})\text{-}\mathbf{M^H}{\cdot}(\boldsymbol{S})\text{-}\mathbf{M^H}{\cdot}H]^+$ (generated from

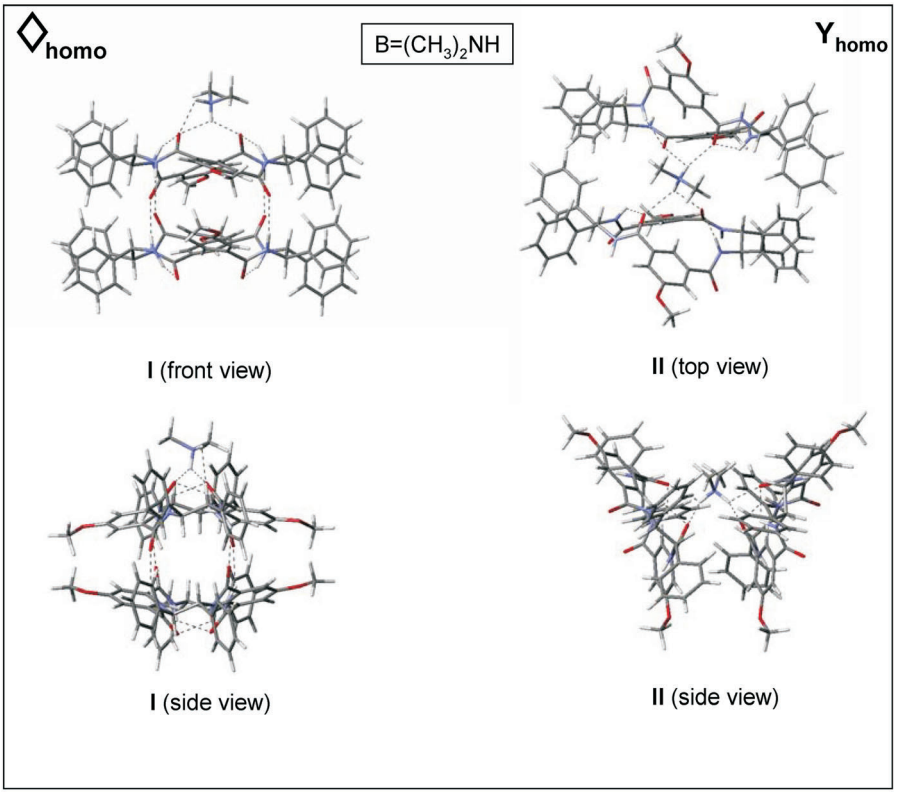

FIG. 9
(*Continued*)

[(***R***)-$\mathbf{M^H}$·(***S***)-$\mathbf{M^H}$·H·CH_3NH_2]$^+$ by loss of neutral CH_3NH_2) is 2.1 kcal/mol lower in energy than its homochiral counterpart [((***R***)-$\mathbf{M^H}$)$_2$·H]$^+$ (generated from [((***R***)-$\mathbf{M^H}$)$_2$·H·CH_3NH_2]$^+$ by loss of CH_3NH_2). On these grounds, base release from [(***R***)-$\mathbf{M^H}$·(***S***)-$\mathbf{M^H}$·H·CH_3NH_2]$^+$ is computed to be 1.3 kcal/mol less endothermic than the same process from [((***R***)-$\mathbf{M^H}$)$_2$·H·CH_3NH_2]$^+$. These results are in agreement with the results of Table I pointing to a more extensive base release from the heterochiral [$\mathbf{M^H}$·$\mathbf{M^D}$·H·CH_3NH_2]$^+$ adducts relative to the homochiral [($\mathbf{M^X}$)$_2$·H·CH_3NH_2]$^+$ ones.

Calculations carried out on complexes containing $(CH_3)_2NH$ as the base revealed a preference for the more stable homochiral adducts with the

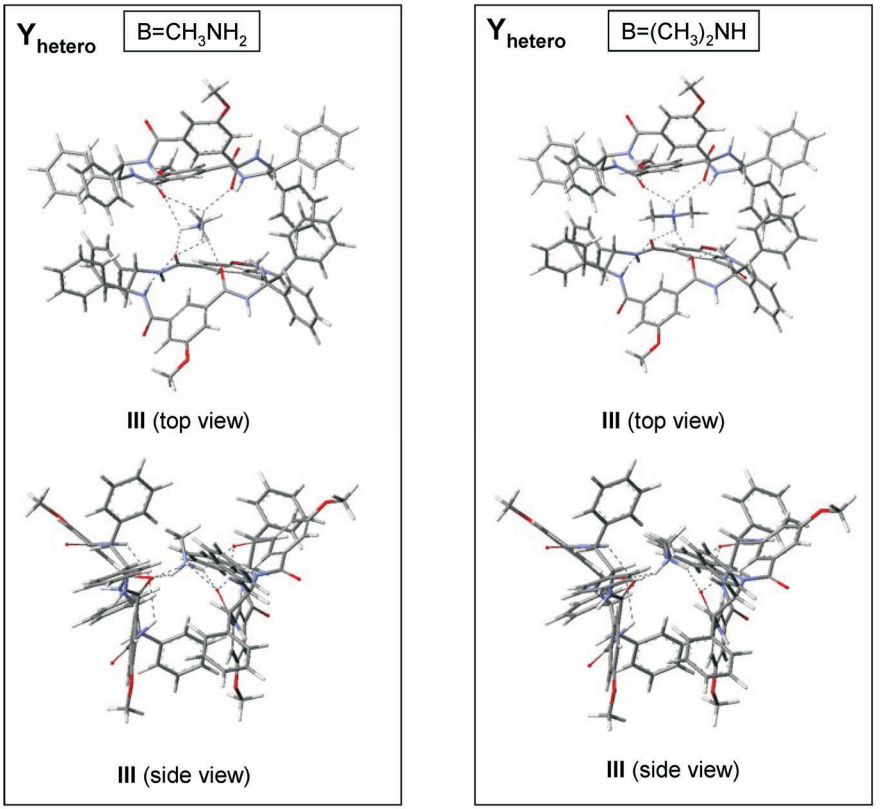

FIG. 9
(*Continued*)

$\Diamond_{\mathbf{homo}}$ geometry, with a Boltzmann population of 93%. The inverted stability order found for the homochiral adducts changing the base from CH_3NH_2 to $(CH_3)_2NH$ may be easily rationalized in terms of steric effects. Relative to CH_3NH_2, the presence of an additional methyl group in $(CH_3)_2NH$ hampers its complexation with the $\mathbf{Y}_{\mathbf{homo}}$ geometry in favour of the $\Diamond_{\mathbf{homo}}$ one[23], where the amine is not constrained in the limited space between the two facing guest and can be more easily accommodated on the outer F2 side of one of the hosts. A similar steric effect is not observed for the heterochiral complex. In this case, in fact, the conceivable $\Diamond_{\mathbf{hetero}}$ supramolecular disposition is not possible, as the amidic functionalities of the facing enantiomeric hosts have opposite H-bond directionality. Because of that, the macrocyclic units have to slide over each other to allow H-bondings between just a single couple of facing -CO-NH- groups placed on the outer margins of the concave sides F1. Calculations indicated that the $\mathbf{Y}_{\mathbf{hetero}}$ geometry is in this case slightly less stable than the $\Diamond_{\mathbf{homo}}$ one by 0.6 kcal/mol. Experimental support to this stability difference is provided by the slightly more extensive loss of a host molecule observed from CID of $[\mathbf{M}^{\mathbf{H}}\cdot\mathbf{M}^{\mathbf{D}}\cdot H\cdot(CH_3)_2NH]^+$ as compared to that from CID of $[(\mathbf{M}^{\mathbf{X}})_2\cdot H\cdot(CH_3)_2NH]^+$.

The extensive release of CH_3NH_2 (Table I), as compared to $(CH_3)_2NH$ (Table II), from the relevant homochiral $[(\mathbf{M}^{\mathbf{X}})_2\cdot H\cdot B]^+$ complexes can be attributed not only to their different geometries ($\mathbf{Y}_{\mathbf{homo}}$ vs $\Diamond_{\mathbf{homo}}$, respectively), but also to the different proton affinities of the amine B. CID-promoted extrusion of CH_3NH_2 from the homochiral structure $\mathbf{Y}_{\mathbf{homo}}$ may be favoured by its low proton affinity (PA = 214.9 kcal/mol)[24] and by the formation of a very stable $[(\mathbf{M}^{\mathbf{X}})_2\cdot H]^+$ structure wherein the extra-proton coordinates the converging pairs of carbonyls placed on the convex sides F2 of two facing host molecules. The comparatively high PA of $(CH_3)_2NH$ (PA = 222.2 kcal/mol)[24] hinders its CID-promoted loss from the homochiral structure $\Diamond_{\mathbf{homo}}$ in favour of the competing loss of a host molecule. In this way, an intense coordination of the onium ions with the converging carbonyls located on the convex sides F2 of the residual host molecule is maintained. Given the strict similarity of the most stable structures $\mathbf{Y}_{\mathbf{hetero}}$ for the heterochiral $[\mathbf{M}^{\mathbf{H}}\cdot\mathbf{M}^{\mathbf{D}}\cdot H\cdot B]^+$ complexes (Fig. 9), the pronounced effect of the amine B on their fragmentation patterns is to be attributed almost exclusively to the different PA of the amine.

CONCLUSIONS

The present MS and computational study provides some pieces of information on the structure, the relative stability, and the CID patterns of the proton-bound homochiral and heterochiral complexes, formed by the combination of two molecules of a chiral macrocyclic tetra-amide with identical or opposite configurations and an amine B (CH_3NH_2, $(CH_3)_2NH$, or (*S*)-(–)-1-phenylethylamine). The collision-induced dissociation (CID) of these complexes has been investigated in the gas phase by ESI-ITMS-CID mass spectrometry. With B = CH_3NH_2, the CID pattern is characterized by the predominant loss of B, accompanied by a much less extensive release of one host molecule. With (*S*)-(–)-1-phenylethylamine, loss of the host efficiently competes with loss of B. Finally, with $(CH_3)_2NH$, loss of the host predominates over loss of B. No appreciable isotope and chiral guest configuration effects have been detected in the fragmentation of the homochiral complexes. A distinct configurational effect has been appreciated in the CID of the homo- and the heterochiral complexes with all amines used. Detailed molecular modeling calculations are in full agreement with the experimental findings. The differences in the CID patterns of the homo- and the heterochiral complexes have been rationalized in terms of structural factors and of the basicity of amine B.

Supporting Information Available

Comparative plots of the relative abundances of the products from CID of the homochiral $[(M^{\mathbf{X}})_2 \cdot H \cdot B]^+$ (X = H, D) complexes from ESI of the (***S***)-$\mathbf{M^H}$/(***R***)-$\mathbf{M^D}$/B mixtures. This material is available free of charge at http://dx.doi.org/10.1135/cccc2008155.

This work was supported by the Ministero dell'Istruzione dell'Università e della Ricerca (MiUR-COFIN) and ASI (Grant No. NI/015070).

REFERENCES AND NOTES

1. Lehn J.-M.: *Supramolecular Chemistry. Concepts and Perspectives*. Wiley-VCH, Weinheim 1995.
2. Beer P. D., Gale P. A., Smith D. K.: *Supramolecular Chemistry* (Oxford Chemistry Primers, 74). Oxford University Press, Oxford 1999.
3. Schneider H.-J., Yatsimirsky A.: *Chem. Soc. Rev.* **2008**, *37*, 263.
4. Steed J. W., Atwood J. L.: *Supramolecular Chemistry*. Wiley, New York 2000.
5. Hollfelder F., Kirby A. J., Tawfik D. S.: *Nature* **1996**, *383*, 60.

6. For a recent reviews on gas-phase enantioselectivity, see: a) Speranza M.: *Int. J. Mass Spectrom.* **2004**, *232*, 277; b) Speranza M.: *Adv. Phys. Org. Chem.* **2004**, *39*, 147.
7. Filippi A., Gasparrini F., Pierini M., Speranza M., Villani C.: *J. Am. Chem. Soc.* **2005**, *127*, 11912.
8. Gasparrini F., Pierini M., Villani C., Filippi A., Speranza M.: *J. Am. Chem. Soc.* **2008**, *130*, 522.
9. Cooks R. G., Kruger T. L.: *J. Am. Chem. Soc.* **1977**, *99*, 1279.
10. McLuckey S. A., Cameron D., Cooks R. G.: *J. Am. Chem. Soc.* **1981**, *103*, 1313.
11. Cooks R. G., Patrick J. S., Kotiaho T., McLuckey S. A.: *Mass Spectrom. Rev.* **1994**, *13*, 287.
12. Cooks R. G., Koskinen J. T., Thomas P. D.: *J. Mass Spectrom.* **1999**, *34*, 85.
13. Armentrout P. B.: *J. Am. Soc. Mass Spectrom.* **2000**, *11*, 371.
14. Dang T. T., Pedersen S. F., Leary J. A.: *J. Am. Soc. Mass Spectrom.* **1994**, *5*, 452.
15. Yao Z., Wan T. S. M., Kwong K., Che C.: *Chem. Commun.* **1999**, *20*, 2119.
16. Tao W. A., Zhang D., Wang F., Thomas P., Cooks R. G.: *Anal. Chem.* **1999**, *71*, 4427.
17. Splitter J. S., Turecek F. (Eds): *Applications of Mass Spectrometry to Organic Stereochemistry*. VCH Publishers, Inc., New York 1994.
18. Turecek F.: *Top. Curr. Chem.* **2003**, *225*, 77.
19. Alcaro S., Gasparrini F., Incani O., Mecucci S., Misiti D., Pierini M., Villani C.: *J. Comput. Chem.* **2000**, *21*, 515.
20. Angelini G., Cerichelli G., Cerritelli S., Pierini M., Siani G., Villani C.: *J. Comput.-Aided Mol. Des.* **2005**, *19*, 259.
21. Alcaro S., Gasparrini F., Incani O., Caglioti L., Pierini M., Villani C.: *J. Comput. Chem.* **2007**, *28*, 1119.
22. Schröder D., Schwarz H.: *Int. J. Mass Spectrom.* **2004**, *231*, 139.
23. This effect is witnessed by the significant increase of the distances δ between the N-H center of the onium ion and the O atoms of the host F2 carbonyls in $\mathbf{Y_{homo}}$ when $CH_3NH_3^+$ (2.773 Å < δ < 2.925 Å) is replaced by $(CH_3)_2NH_2^+$ (2.884 Å < δ < 3.015 Å).
24. http://webbook.nist.gov/chemistry/name-ser.html